WILEY | Hindawi

Research Article

Study on Damage Evolution of Tunnel Lining under Strike-Slip Fault Movements

Jiaxuan Du [ID],[1] **Songhong Yan** [ID],[1] **Weiyu Sun** [ID],[2] **Mingxing Cao** [ID],[1] **Yuxiang Li** [ID],[1] **and Kang Yang** [ID][1]

[1]*School of Civil Engineering, Lanzhou Jiaotong University, Lanzhou 730070, China*
[2]*Key Laboratory of Road & Bridge and Underground Engineering of Gansu Province, Lanzhou Jiaotong University, Lanzhou 730070, China*

Correspondence should be addressed to Songhong Yan; yansonghong@mail.lzjtu.cn

For the purpose of investigating the damage mechanism and failure characteristics of tunnel lining under the strike-slip fault movements, a three-dimensional elastoplastic finite element model was established in the present study including a railway tunnel across an active strike-slip fault. With the assistance of this numerical model, the tensile and compressive damage, plastic strain development process, and shear failure of the secondary lining at different fault plane positions were analyzed, and further, the damage laws of the secondary lining at different fault displacement and tunnel-fault intersection angles were summarized. The simulation results showed that when the maximum imposed fault displacement is 30 cm, the most unfavorable fault plane appears at the junction between the moving block and the fracture zone, and serious tensile cracks and shear failures occur on each fault rupture plane. Besides, the maximum plastic strain and compressive damage are distributed in the vault and invert. In addition, with the increase of the fault displacement, the axial strain of the secondary lining increases as well, of which the main part shows the tensile strain. Interestingly, with the decrease of the crossing angle, the axial strain gradually changes from the tensile strain to the compressive strain, which is consistent with the direction of the fault angle. Furthermore, the tensile and compressive damage of the secondary lining increases with the increase of movement distance. At the same time, the tensile damage along the tunnel ring develops, and the compressive damage propagates mainly in tunnel vault and invert. With the decrease of the crossing angle, the degree of the tensile damage in the lining reduces, as well as its range. The compressive damage area of the lining develops from the vault and inverted arch to the tunnel wall on both sides, which has a trend of penetrating the side walls on both sides. The distribution area and maximum value of the overall lining damage indices in tensile (OLDT) and overall lining damage indices in compressive (OLDC) increase with the increase of fault movement distance. With the decrease of the crossing angle, the distribution range and maximum value of OLDT decrease, and the distribution range of OLDC increases, while the maximum value basically remains the same. The research results of the present work can provide reference for the antidislocation design of railway tunnels crossing strike-slip faults.

1. Introduction

Fault fracture zone is often encountered in mountain tunnel construction adverse geological conditions. Fault fracture zone area is usually considered to contain a large amount of groundwater, due to the existence of geological fluid. This may lead to water inrush collapse and other accidents in the construction process of crossing the fault tunnel, which affects construction safety and construction quality [1]. There have been a lot of research results on the mechanism and classification of tunnel water inrush [2–4]. On the other hand, the earthquake damage example [5] shows that fault dislocation is the most harmful to tunnel engineering. The cumulative displacement of creep slip dislocation of active faults will make tunnel lining crack, concrete spalling, water leakage, and even collapse in serious cases. The groundwater

in the fault fracture zone will also aggravate the damage degree of tunnel lining. When studying the reaction law of tunnel engineering under the action of fault dislocation, the key is to formulate reasonable antidislocation measures, and the basis is to ensure the safe operation of tunnel engineering. Therefore, it is of great significance to carry out the research on the damage law of tunnel lining caused by fault dislocation.

The current research methods mainly include model test and numerical simulation. For example, by using model test, Liu and Lin and Liu et al. [6, 7] carried out the model tests with the scale of 1 : 50 and three fault dip angles of 45°, 60°, and 75° and studied the strain distribution of tunnel lining under normal fault movement. Besides, Yan et al. [8] tested the articulated design of cross-fault tunnel through scale model test, and it was shown that the adjustment of articulated joint length could effectively control the tensile damage range of lining. In addition, Liu et al. [9] adopted a new experimental device to simulate fault creep slip. The test system installed 3D loading function, variable angle sliding mechanism, and flexible loading device with air bag and air spring and obtained the deformation and failure characteristics of tunnel lining under creep slip; the study is helpful to provide the basis for the design of tunnel structure through deep buried active faults. The above research clarifies the damage characteristics of fault dislocation to tunnels, and its results provide some reference for the construction of tunnels crossing active faults. However, the current model test research is based on small-scale physical model tests, and the geometric similarity ratio is mostly less than 1 : 40. Due to the limitation of boundary effects, the research results often have limitations.

In terms of numerical simulation, Chermahini and Tahghighi [10] studied the influence of tunnel position, fault dip angle, and lining thickness on fault dislocation on tunnel structure by adopting 2D finite element analysis method and further studied the influence of the intersection angle of fault and tunnel and mechanical properties of soil around tunnel and fault dip angle on tunnel stability through the analysis of 3D finite element model. Besides, Wang et al. [11] applied the cohesive interface model of fracture mechanics in the simulation of normal fault fracture and numerically analyzed the influence rules of different fault displacement and dip angles on lining damage. Based on the ABAQUS finite element model, An et al. [12, 13] studied the damage evolution of tunnel lining under the action of reverse fault movement and analyzed the influence of tunnel bottom distance from the fault plane and the width of fracture zone. Similarly, Han and Li [14] studied the influence of the segment length, section shape, and lining thickness of articulated lining on the antidislocation effect of the tunnel by numerical simulation method, which takes the railway tunnel crossing the reverse fault as the background. What is more, Ma et al. [15] established a 3D finite element model based on an actual tunnel in southwest China and revealed the fault dislocation failure mechanism of the tunnel from the parameters of tunnel lining deformation, stress distribution, and plastic zone distribution. The above research results are mostly based on the analysis of the axial stress

and strain distribution of the tunnel and the deformation law of the tunnel, and less attention is paid to the damage evolution law of the tunnel. In addition, the numerical simulation of tunnels is mostly set as elastic constitutive model, which cannot consider the stiffness degradation of concrete in the plastic stage, and its research results have certain limitations. Besides, the research background is mostly based on normal or thrust faults, and there are few reports on strike-slip faults.

In view of the shortcomings of existing research results, this paper adopts the finite element numerical simulation method based on concrete damage plasticity model in ABAQUS software, to carry out research on the damage characteristics of tunnel lining across active faults and to explore the damage evolution of tunnel lining under different fault plane positions, fault displacement distances, and tunnel-fault angles. It is expected to provide a reference for the relevant research and engineering design of tunnels crossing active faults.

2. Engineering Background and Finite Element Model

2.1. Engineering Background. The length of the tunnel is 12323.1 m. The maximum buried depth is 1525.4 m, and it is a single-hole double-line tunnel. The prototype of the tunnel was constructed by drilling and blasting method, and the tunnel section is nearly round. The lining system is composed of primary support and secondary lining. The thickness of the primary support is 0.25 m, and the concrete strength grade is C30. The thickness of the secondary lining is 0.60 m, and the concrete strength grade is C35. The preliminary figuration of the cross-sectional supporting structure of the tunnel is shown in Figure 1. There are multiple geologic types existed in the tunnel, and the near exit section passes through the F48 active fault, of which the width of fault fracture zone is 415 m. The latest GPS observation results of the Institute of Geology, China Earthquake Administration, show that the current activity of the F48 active fault is mainly strike-slip movement, and the movement rate is about 2~3 mm/a. The fault fracture zone is mainly composed of fault gouge, cataclastic rock, altered rock, and melange rock.

2.2. Finite Element Model and Parameter Selection. The nonlinear finite element model was established in the general finite element program ABAQUS software, and the damage evolution of the tunnel lining and the response of the tunnel structure under creep dislocation of strike-slip fault are simulated. The three-dimensional finite element numerical model of fault plane at the junction of movable disk and fracture zone is shown in Figure 2, and the intersection angle between tunnel and fault is 90°. After several trials of calculation, it was found that when the distance between the center line of the tunnel and the upper free surface was 100 m, the influence of the boundary on the tunnel response could be ignored. Therefore, the size of the model was calculated by taking 1000 m along the tunnel axis (Z-axis direction), 200 m along the left and right sides (X-axis direction), and
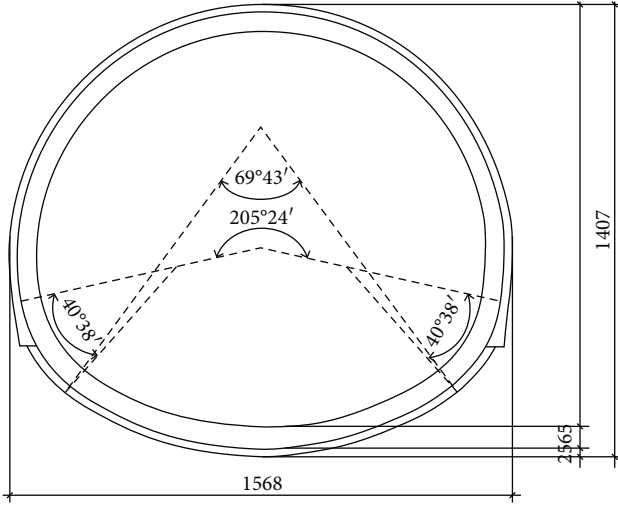
Figure 1: Tunnel support structure.

200 m along the upper and lower sides (Y-axis direction) of the tunnel center. In order to comprehensively consider the calculation efficiency and accuracy, only the part of the model close to the fault fracture zone was divided into finer meshes, while the rock mass far from the fault fracture zone was coarser. Similarly, at the intersection between the tunnel and the fault plane, the vertical mesh of 100 m along the tunnel is also finer, and the size of the vertical mesh is 1.0 m.

In the simulation, it is simply assumed that the rock mass and fault fracture zone have good homogeneity, and the material properties remain unchanged. The inhomogeneity of rock mass and rock mass joints is not considered in this paper. The constitutive model of complete rock mass and fracture zone is the Mohr-Coulomb ideal elastic-plastic model. The reduced integral C3D8R hexahedron solid element is selected for rock mass medium and tunnel structure. Physical and mechanical parameters of rock were selected based on on-site geological prospecting data and *Engineering Rock Mass Classification Standard (GB/T50218-2014)* [16], and the parameters are shown in Table 1. Although lining concrete with linear elastic constitution can better reflect the influence law and change trend of structure under the influence of different parameters, it cannot consider the stiffness degradation of concrete at the plastic stage, nor can it quantitatively express the failure state of lining concrete. Concrete damaged plasticity model (CDP model) in ABAQUS can reflect the phenomenon of tensile cracking and crushing of concrete materials in the plastic stage, so CDP model is adopted in the numerical simulation of lining constitutive model.

CDP model is divided into two parts: (1) the stress strain curve of concrete under compressive and tensile loading, respectively, and (2) the damage parameters d_t and d_c under tensile and compressive. Its stress-strain curve follows the following law:

The formulas for tensile state are shown as

$$\sigma = (1 - c_t)E_c\varepsilon, \tag{1}$$

$$c_t = \begin{cases} 1 - \rho_t[1.2 - 0.2x^5], & x \le 1, \\ 1 - \dfrac{\rho_t}{\alpha_t(x-1)^{1.7} + x}, & x > 1, \end{cases} \tag{2}$$

$$x = \frac{\varepsilon}{\varepsilon_{t,r}}, \tag{3}$$

$$\rho_t = \frac{f_{t,r}}{E_c\varepsilon_{t,r}}, \tag{4}$$

where E_c is Young's modulus, c_t is the evolution parameter of tensile damage, α_t is the parameter value of the descending section of the uniaxial tensile curve of concrete, $f_{t,r}$ is the representative value of the uniaxial tensile strength of concrete, $\varepsilon_{t,r}$ is the peak tensile strain corresponding to $f_{t,r}$, x is the variable, and ρ_t is the parameter in the derivation process.

The formulas for compressive state are shown as

$$\sigma = (1 - c_c)E_c\varepsilon, \tag{5}$$

$$c_c = \begin{cases} 1 - \dfrac{\rho_c n}{n - 1 + x^n}, & x \le 1, \\ 1 - \dfrac{\rho_c}{\alpha_c(x-1)^2 + x}, & x > 1, \end{cases} \tag{6}$$

$$x = \frac{\varepsilon}{\varepsilon_{c,r}}, \tag{7}$$

$$n = \frac{E_c\varepsilon_{c,r}}{E_c\varepsilon_{c,r} - f_{c,r}}, \tag{8}$$

$$\rho_c = \frac{f_{c,r}}{E_c\varepsilon_{c,r}}, \tag{9}$$

where c_c is the compressive evolution coefficient, α_c is the parameter value of the descending section of the uniaxial compressive curve of concrete, $f_{c,r}$ is the unit value of the uniaxial compressive strength of concrete, $\varepsilon_{c,r}$ is the peak compressive strain corresponding to $f_{c,r}$, n and x are variables, and ρ_c is the parameter in derivation process.

The damage factors d_t and d_c are derived from the energy equivalence principle, as shown in

$$\begin{cases} d_t = 1 - \sqrt{\rho_t(1.2 - 0.2x^5)}, & x \le 1, \\ d_t = 1 - \sqrt{\dfrac{\rho_t}{\alpha_t(x-1)^{1.7} + x}}, & x > 1, \end{cases} \tag{10}$$

$$\begin{cases} d_c = 1 - \sqrt{\dfrac{\rho_c n}{n - 1 + x^n}}, & x \le 1, \\ d_c = 1 - \sqrt{\dfrac{\rho_c}{\alpha_c(x-1)^2 + x}}, & x > 1. \end{cases} \tag{11}$$

The elastoplastic stress-strain relationship of lining concrete adopts the model proposed in *Code for Design of Concrete Structures (GB50010-2010)* [17], and the relevant parameters are listed in Table 2. The primary support of
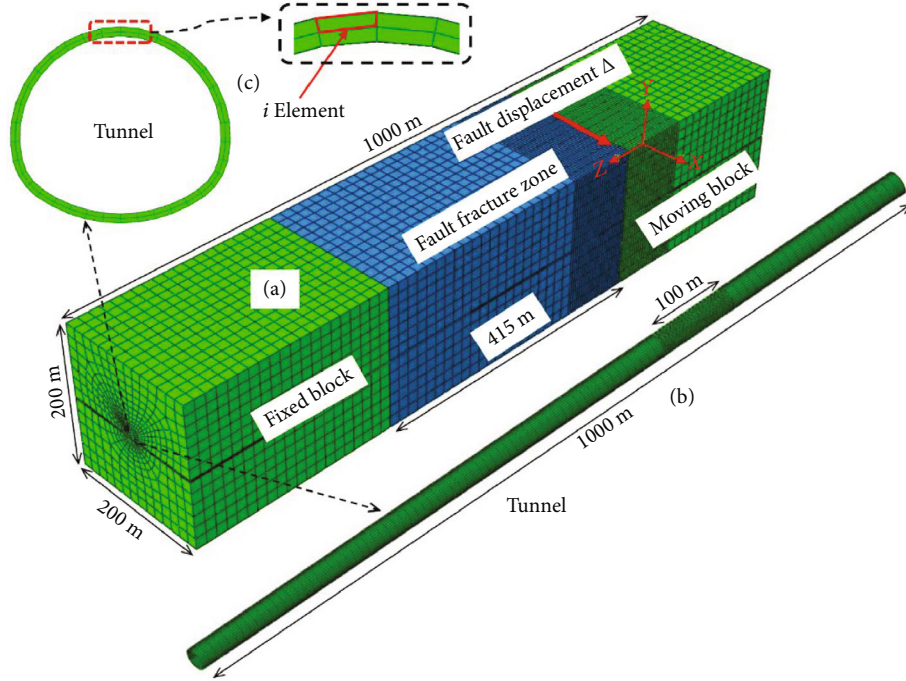
Figure 2: The diagram of calculation model. (a) Overall calculation model. (b) Tunnel lining. (c) Schematic diagram of i element.

Table 1: Rock mechanical parameters.

Name	Density (kg/m³)	Elastic modulus (GPa)	Poisson ratio	Internal friction angle (°)	Cohesion (MPa)
Competent rock mass	2 100	3.0	0.33	31	0.40
Fault fracture zone	1 700	1.1	0.41	21	0.07

Table 2: Mechanical parameters of lining.

Name	Density (kg/m³)	Elastic modulus (MPa)	Poisson ratio	Compressive yield stress (MPa)	Tensile yield stress (MPa)
Primary support	2 400	30 000	0.2	20.1	2.01
Secondary lining	2 500	31 500	0.2	23.4	2.20

tunnel is constructed using drilling and blasting method, which mainly consists of sprayed concrete and anchor, and if it is necessary, pipe roof and steel arch are also needed to reinforce the surrounding rock. Therefore, there is close contact between the primary support and surrounding rock, and considering the deformation of surrounding rock deformation, the contact between primary support and surrounding rock is set to the binding constraint of ABAQUS.

The interaction between the primary support and the secondary lining is modeled by contact surface mechanics. The contact setting between the primary support surface and the secondary lining surface can realize the relative slip (including normal and tangential displacement) and contact force transmission between linings during fault dislocation, so as to reflect the interaction relationship between linings more truly. In the normal direction of the interface, "hard contact" is adopted; that is, the normal direction of the interface can only transfer contact pressure and does not limit the value of contact pressure. When the contact pressure between the primary support and the secondary lining

becomes 0 or negative, the contact constraint on the corresponding node is released at the same time. The tangential mechanical behavior of the interface is based on Coulomb's law of friction, and the penalty stiffness algorithm is used to allow elastic slip deformation. When the tangential contact shear stress exceeds the critical value, the relative slip will occur between the primary support and the secondary lining, and the value of friction coefficient is 0.4 [18], and the friction contact coefficient between the fault fracture zones and the moving block is set as 0.1 [19].

The numerical simulation can be divided into the following three steps: (1) Gravity is applied to the model as a whole to achieve balance of the initial ground stress. (2) The "softening modulus method" is adopted to simulate tunnel excavation. During the simulated construction process, the effect of stress release during tunnel excavation can be realized by softening the elastic modulus of rock mass in the tunnel and activating the lining at the same time. (3) Displacement along the fault direction is applied to the external nodes of the moving disk to realize dislocation.

2.3. Verification of Numerical Method. Before further analysis, the reliability of the numerical model needs to be verified. The numerical simulation method in this paper is used to check the test results in reference [20]. The test background in reference [20] is similar to the engineering background in this paper, so the verification results are referential. In the background, the tunnel contour is circular, and the tunnel ellipticity is used to measure the deformation degree of the tunnel section. The positive/negative ellipticity represents the flattening/narrowing of the tunnel section. The finite element model was established by using rock mass parameters and lining parameters. Under the action of strike-slip fault dislocation of 25 mm, the lining ellipticity measured in the finite element simulation of lining ellipticity test was compared, as shown in Figure 3, where the abscess $X > 0$ represents the direction of the moving block. $X < 0$ represents the direction of the fixed block, where $X = 0$ is the fault rupture plane. It can be seen that the finite element analysis results are in good agreement with the test results, and the deformation trend of the lining is consistent, which verifies the validity of the numerical model.

3. Damage Analysis of Tunnel Lining by Different Fault Planes

Fault rupture plane generally exists in the fault fracture zones, but it is hard to exactly predict the detailed position [21]. The damage degree of tunnel structure may be different with various rupture plane locations. Considering the wide width of fault fracture zone (415 m) in the studied project, in order to analyze the damage degree of tunnel structure caused by various rupture plane locations, rupture plane 1 was set up in the interface between the moving block and fault fracture zone, rupture plane 2 occurred in the middle of fault fracture zone, and rupture plane 3 appeared in the interface between fault fracture zone and fixed block, on three kinds of circumstances in 100a maximum of 30 cm right-lateral strike-slip displacement; the schematic diagram of the rupture planes at three different positions are shown in Figure 4.

Table 3 shows the distribution cloud diagram of tensile and compression damage, equivalent plastic strain (PEEQ), and shear strain of the secondary linings under three different modes of rupture. Figure 5 shows the comparison of the maximum value of each damage index. It can be seen that under the action of creep and strike-slip fault movement, the tunnel structure is seriously damaged due to the complex combination of tension, compression, bending, and shear. As can be seen from Figure 5 and Table 3, all damage indexes of the rupture plane 1 are the largest, indicating that under the condition of the same rupture distance, the damage degree of the tunnel structure is the most serious in the case of the rupture plane 1, followed by the rupture plane 3, and the damage index of the rupture plane 2 is the smallest. Therefore, the rupture plane 1 is the most unfavorable rupture under the three kinds of rupture.
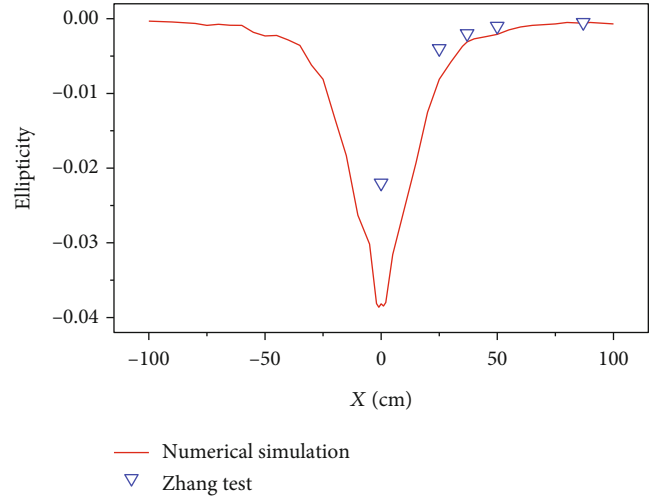

FIGURE 3: Comparison between finite element simulation and experimental results in reference [20].

3.1. Analysis of Tensile Crack in Lining with Different Rupture Planes. It can be seen from the distribution cloud diagram in Table 3 that the tensile damage on all the rupture planes basically distributed at the same region, and the tensile damage on both side walls and the arch waist is more serious. Chen et al. [22] proposed a reasonable calculation formula for concrete cracks based on tensile damage factor, and the formula is shown in

$$d_t = \frac{w_t}{[w_t + (\sigma_t h_c)/E_0]}, \qquad (12)$$

where h_c is the length of characteristic value, which is equal to the side length of the grid cell, σ_t is the tensile stress, and E_0 is the initial elastic modulus of concrete.

In the Code for Design of Hydraulic Concrete Structures (SL 191-2008) [23], it is defined that concrete members with tensile crack width greater than 0.2 mm are in the serious damage state. According to Equation (12), it can be calculated that the corresponding tensile damage factor is 0.74, when the tensile crack width of the secondary lining concrete (C35) is 0.2 mm. Therefore, both sides of the side wall and the secondary lining of the arch waist of the rupture plane have serious tensile damage.

3.2. Analysis of Compressive Damage of Lining at Different Rupture Planes. According to the distribution cloud diagram of compressive damage on each rupture plane, the distribution of compressive damage factors is basically the same in the vault and invert and tends to develop to the left- and the right-side walls. The maximum compression damage factors are distributed near the fault plane. Taking rupture plane 1 as an example, Figure 6 shows the compressive damage factor distribution cloud obtained by numerical simulation; when the fault rupture distance is 30 cm, the secondary lining arch and invert were deformed excessively due to the dislocation of the fault, and the secondary lining invert and vault were deformed obviously under pressure, which may
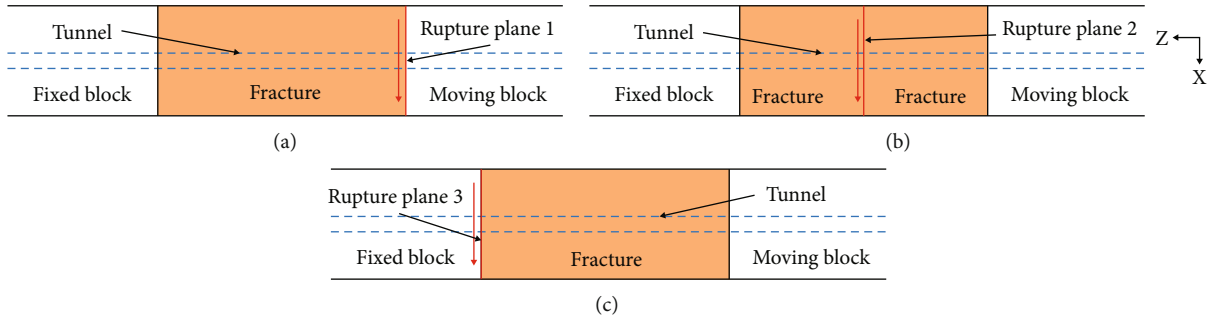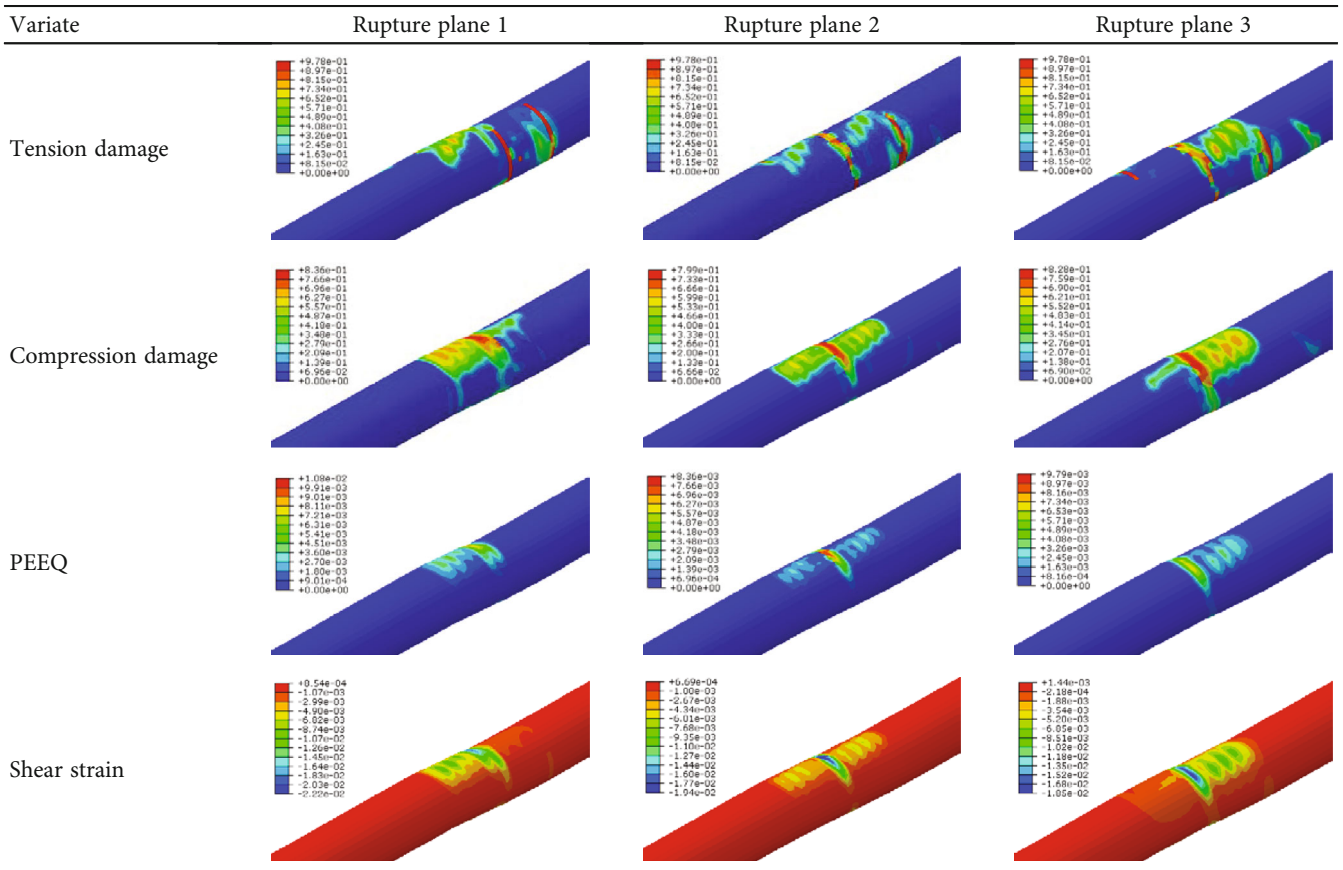
Figure 4: Schematic diagram of the different rupture planes. (a) Rupture plane 1. (b) Rupture plane 2. (c) Rupture plane 3.

Table 3: Secondary lining damage index distribution on different rupture plane.

Variate	Rupture plane 1	Rupture plane 2	Rupture plane 3
Tension damage			
Compression damage			
PEEQ			
Shear strain			

lead to the partial falling or even collapse of the tunnel lining across the fault plane.

3.3. Analysis of PQQE Development Process of Lining at Different Rupture Planes. It can be known from the plastic strain distribution cloud diagram that when the fault displacement reaches 30 cm, the PQQE of lining is mainly concentrated in the vault and invert, which means that the secondary lining concrete has been seriously yielded. Taking the rupture plane 1 as an example, Figure 7 shows the local cloud diagram of the PQQE development process of the secondary lining concrete under different fault displacement Δ. As shown in Figure 7, it can be seen that when the fault displacement is less than 1.5 cm, the secondary lining does not present plastic strain, and the secondary lining concrete does not yield at this time. With the increase of the fault displacement, the PQQE first appears at the waist and foot of the secondary lining arch and then gradually develops to the vault and invert. When the fault displacement increases to 12 cm, the plastic strain along the Z-axis is the direction of the tunnel longitudinal direction from fault plane development in the direction of fracture zone, which gradually accumulates. When the fault displacement reached the maximum 30 cm within 100a, the maximum plastic strain concentrated in the vault and invert at the fault plane.

3.4. Analysis of Shear Failure of Lining at Different Rupture Planes. According to the shear strain distribution of each
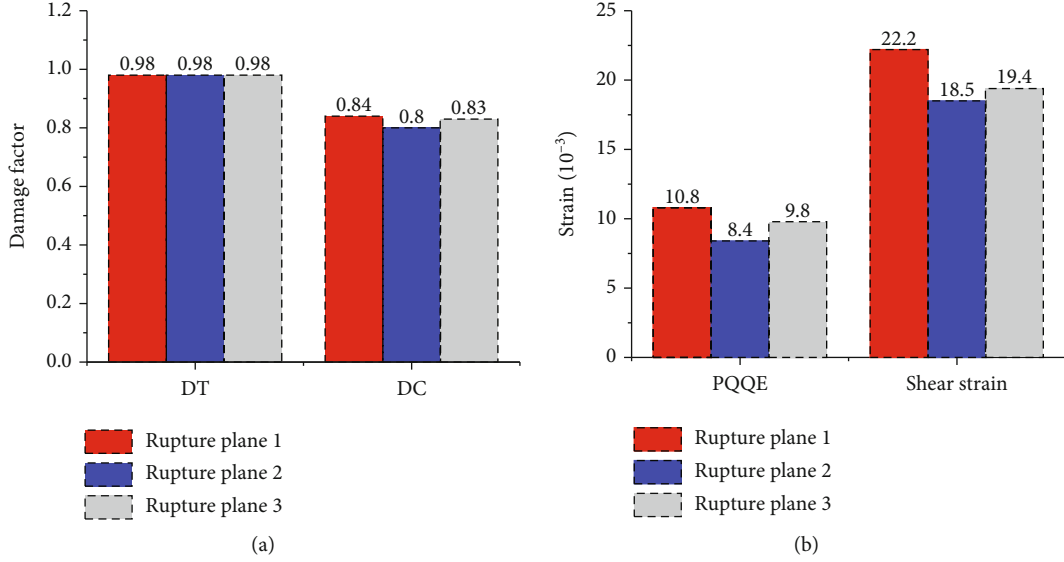
(a)

(b)

Figure 5: Maximum damage index of different rupture plane. (a) Tensile and compressive damage. (b) PQQE and shear strain.
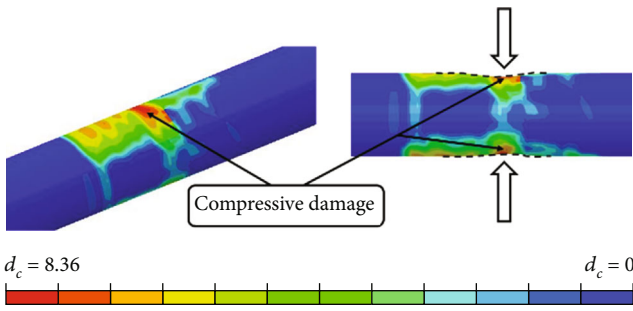

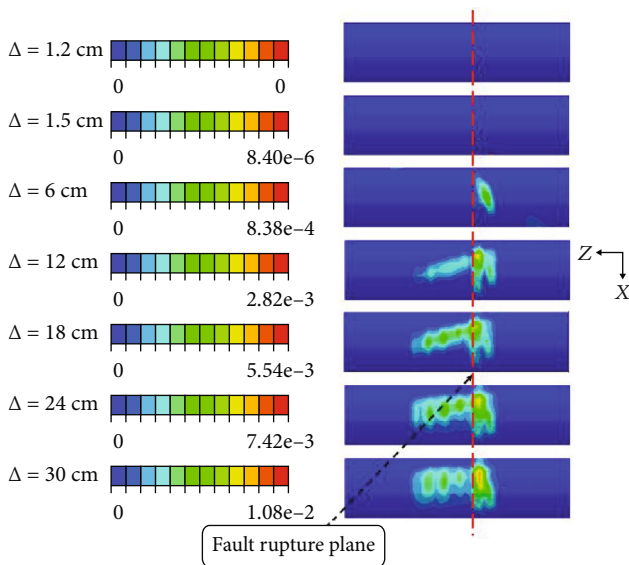Figure 6: Compressive damage factor cloud image.

Figure 7: PQQE development process.

rupture plane, the maximum shear strain is distributed in the secondary lining vault and invert, the ratio of shear strength to compressive strength of concrete is 0.095~0.121 [24], and the shear modulus of concrete is 40% of its elastic modulus [25]. Thus, the ultimate shear strain of C35 concrete can be obtained:

$$\varepsilon_s = \frac{\tau}{G}, \tag{13}$$

where τ is the ultimate shear strength of concrete and G is the shear modulus of concrete.

According to Equation (13), it can be known that the ultimate shear strain of C35 concrete ranges from 1.76×10^{-4} to 2.25×10^{-4}; the maximum shear strains at the arch and invert of different rupture plane are 2.22×10^{-2}, 1.85×10^{-2}, and 1.94×10^{-2}, which are far greater than the ultimate shear strains of C35 concrete, respectively, indicating that serious shear failure is likely to occur in the lining.

4. Damage Analysis of Tunnel Lining by Fault Displacement Distance

The relative dislocation process of faults is also a process of energy release. With the increase of fault displacement, the energy release increases continuously, which leads to the greater damage degree of lining structure. Taking the most unfavorable rupture plane 1 as the analysis basis and the fault dip angle of 90° as the basic analysis model, the axial strain, tension, and compression damage of tunnel lining and the longitudinal distribution of damage of the whole section of tunnel lining under different fault displacement Δ were investigated, and the maximum displacement of the fault is 5 cm, 10 cm, 20 cm, and 30 cm, respectively.

4.1. Influence of Fault Displacement on Axial Strain of Tunnel Lining. Figure 8 shows the axial strains of the tunnel
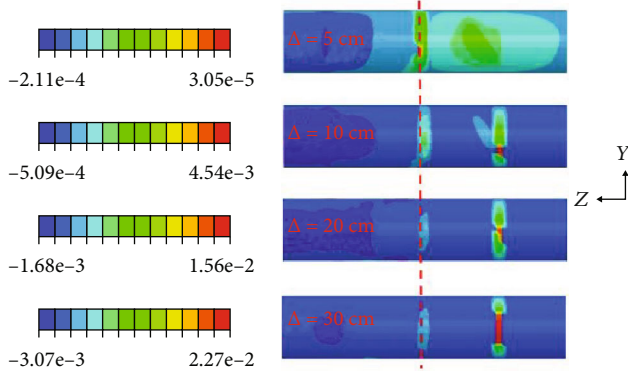
FIGURE 8: Axial strain of tunnel lining under fault displacements.

lining under fault displacement Δ; the red line in the figure indicates the fault plane location, in which positive values represent the tensile strains and negative values represent the compressive strains. It can be seen from this figure that under the strike-slip fault movements, the tunnel lining is mainly subjected to tension along the axial direction, and the maximum tensile strain is distributed at the side wall on both sides of the fault rupture plane, which is consistent with the direction of fault dip angle. Besides, the tensile strain increases with the increase of fault displacement. It shows that the tunnel lining at the side walls on both sides of the fault plane is under strong tensile action.

4.2. Influence of Fault Displacement on Tensile and Compressive Damage of Tunnel Lining.
Figure 9(a) is the tunnel secondary lining under different fault displacement of tensile damage, the letters "R" and "L" represent the right view and the left view of the cloud image. It can be seen from the figure that when the fault displacement $\Delta = 5$ cm, the secondary lining first began to produce vertical tensile damage on the right wall of the tunnel at the fault rupture plane. With the increase of fault displacement, the tensile damage range of the secondary lining gradually develops to both sides of the fault rupture plane, where the tensile damage occurs to the right side wall of the secondary lining within the range of the moving block, and the tensile damage occurs to the left side wall of the secondary lining within the fault fracture zone. The results indicate that the tensile damage of the secondary lining of the tunnel is mainly distributed at the fault rupture plane and the side wall on both sides of the fault rupture plane during the tunnel crossing the 90° strike-slip fault and develops along the tunnel circum-direction.

Figure 9(b) is the tunnel secondary lining under different fault displacement of compressive damage. It can be seen from the figure that when the fault displacement $\Delta = 5$ cm, the secondary lining first began to produce compressive damage at the arch crown and waist at the fault rupture plane. With the increase of fault displacement, the area and degree of compressive damage of the secondary lining at the arch crown and inverted arch gradually developed. When fault displacement $\Delta = 30$ cm, the secondary lining vault and inverted arch at the fault rupture plane have serious compressive damage, and the compressive damage has a trend of penetrating to the side walls on both sides. The results indicate that the com-

pressive damage of the tunnel lining is mainly distributed in the vault and invert near the fault rupture plane during the tunnel crossing the 90° strike-slip fault.

In CDP model, the damage degree of concrete material is represented by tensile damage factor d_t and compressive damage factor d_c, which ranges from 0 to 1.0. When d_t and d_c are both 0, it means that the concrete material is intact; and when they are both 1.0, it presents that the material strength is completely lost. In order to better evaluate the longitudinal distribution characteristics of the overall damage of tunnel lining under the action of strike-slip fault, the evaluation index OLDT (overall lining damage indices in tensile) and the evaluation index OLDC (overall lining damage indices in compressive) of full-section tensile damage and full-section compressive damage of the tunnel lining are adopted in this paper. OLDT and OLDC can be calculated by weighted average d_t factor and d_c factor of each element at each cross-section, by taking the corresponding energy dissipation value of each element as the weighted factor. The calculation formulas are as follows:

$$\text{OLDT} = \sum_{i=1}^{n} \left[d_{ti}^{e} \left(\frac{E_i^e}{\sum_{i=1}^{n} E_i^e} \right) \right], \qquad (14)$$

$$\text{OLDC} = \sum_{i=1}^{n} \left[d_{ci}^{e} \left(\frac{E_i^e}{\sum_{i=1}^{n} E_i^e} \right) \right], \qquad (15)$$

where i is the unit number of the tunnel cross-section, as shown in Figure 2, E_i^e is the dissipated energy of i element, d_{ti}^{e} is the tensile damage value of i element, and d_{ci}^{e} is the compression damage value of i element.

Figure 10(a) shows the longitudinal distribution of OLDT along the tunnel lining under different fault displacement. The abscissa in the figure represents the distance from the fault plane, and the positive direction of Z-axis is positive. According to the distribution of OLDT, with the increase of fault displacement, the damage area of tunnel increases from about 20 m at $\Delta = 5$ cm to about 50 m at $\Delta = 30$ cm, and the damage area increased significantly. With the increase of fault displacement Δ, the maximum value of OLDT increases gradually, from 0.18 when $\Delta = 5$ cm to 0.89 when $\Delta = 30$ cm. From the distribution range of OLDT, the most damaged area is mainly distributed at and on both sides of the fault plane.

Figure 10(b) shows the longitudinal distribution of OLDC along the tunnel lining under different fault displacement. According to the distribution of OLDC, the distribution range of OLDC increases with the increase of fault displacement Δ under the strike-slip fault movements. The damage area of tunnel increases from about 15 m when $\Delta = 5$ cm to about 45 m when $\Delta = 30$ cm, and the damage area increases significantly. With the increase of fault displacement Δ, the maximum value of OLDC increases gradually, from 0.08 at $\Delta = 5$ cm to 0.81 at $\Delta = 30$ cm. From the distribution range of OLDT, the most damaged area is mainly distributed at and on both sides of the fault plane, and the damage area and degree of the tunnel in the fault fracture zones are more significant than that of the moving block.
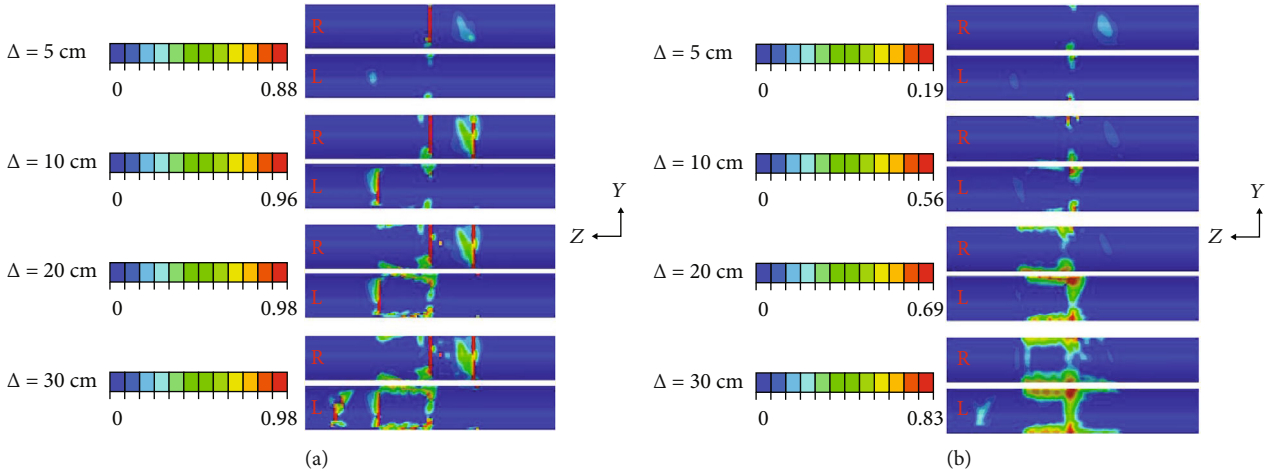
FIGURE 9: Tensile and compressive damage of tunnel lining under different fault displacements. (a) Tensile damage. (b) Compressive damage.
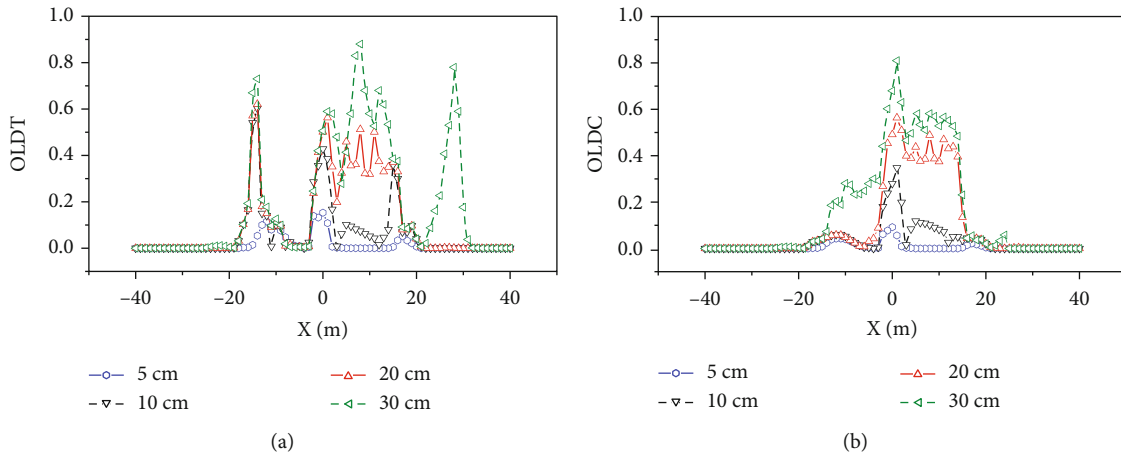

FIGURE 10: Overall lining damage under different fault displacements. (a) OLDT. (b) OLDC.

5. Damage Analysis of Tunnel Lining by Tunnel-Fault Intersection Angle

The intersection angle between the active fault and the tunnel is an important geometric feature of the fault, and the difference in the intersection angle will significantly affect the deformation characteristics and damage characteristics of the tunnel during fault movements. In engineering practice, due to the constraints of route selection, regional geological conditions, and construction costs, mountain railway tunnels often cross-active strike-slip faults at different angles. Based on the analysis of the most unfavorable rupture plane 1, this study selects the tunnel-fault intersection angles to be 50°, 60°, 70°, 80°, and 90°; to analyze the damage law of tunnel lining caused by the intersection angles of tunnel and fault, the fault displacement was taken as the maximum fault displacement of 30 cm within 100a.

5.1. Influence of Tunnel-Fault Intersection Angle on Axial Strain of Tunnel Lining. Figure 11 is the axial strain of the tunnel secondary lining under different tunnel-fault intersection angle; the red line in the figure indicates the fault
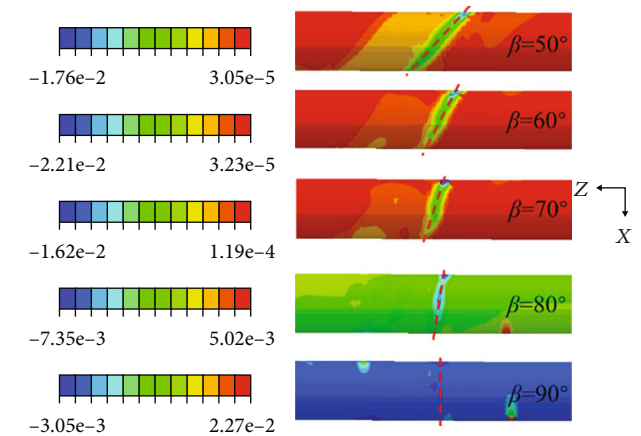

FIGURE 11: Axial strain of secondary linings under different tunnel-fault intersection angles.

plane location. It can be seen that when the tunnel-fault intersection angles are 90° and 80°, the tunnel lining is mainly in tension along the axial direction, and the maximum tensile strain is concentrated at the tunnel side walls

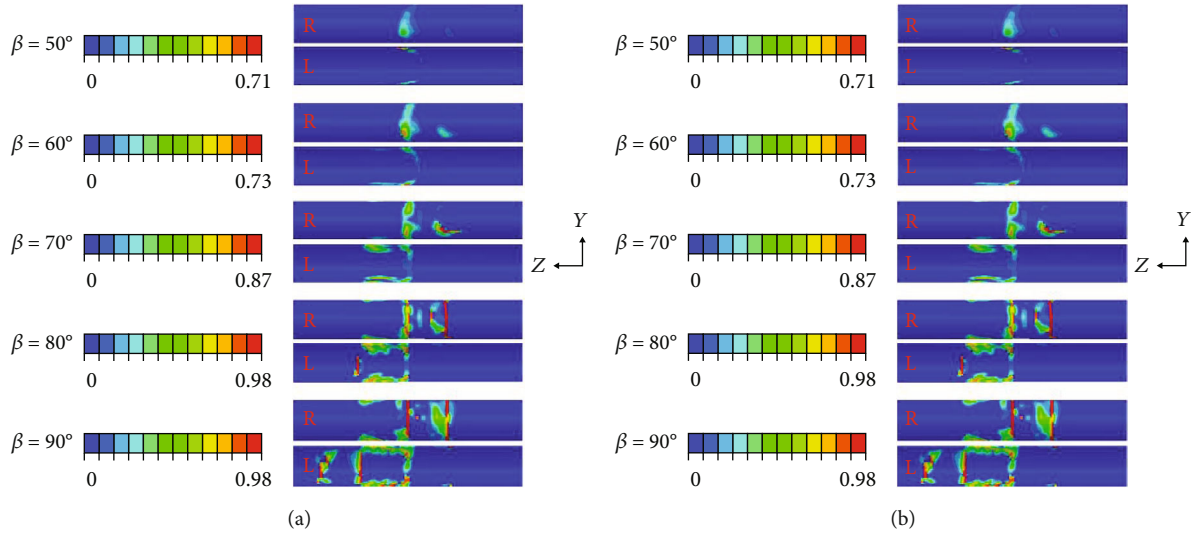(a)   (b)

FIGURE 12: Tensile and compressive damage of secondary lining under different tunnel-fault intersection angles. (a) Tensile damage. (b) Compressive damage.

on both sides of the rupture plane; as the tunnel-fault intersection angle decreases, the axial strain gradually changes from tensile strain to compressive strain, and the compressive strain is mainly distributed at the rupture plane, which is consistent with the fault angle. It shows that with the decrease of the tunnel crossing angle, the axial strain of the tunnel changes from tensile strain to compressive strain.

5.2. Influence of Tunnel-Fault Intersection Angle on Tensile and Compressive Damage of Tunnel Lining. Figure 12(a) shows the tensile damage of the tunnel secondary lining at the different tunnel-fault intersection angles; the letters "R" and "L" represent the right view and the left view of the cloud image. It can be seen that there are obvious differences in the tensile damage of the tunnel when crossing at various angles. When the intersection angle between the tunnel and the fault is 90°, the tunnel is subjected to a large axial tensile stress, so the degree and scope of the tensile damage of the lining are more serious. As the tunnel-fault intersection angle becomes smaller, the tunnel will be subjected to relatively obvious axial compressive stress under the strike-slip fault movements, thereby reducing the extent and scope of the tensile damage of the lining under the strike-slip fault movement. The maximum tensile damage factor from 0.98 at 90° crossing is reduced to 0.72 at 50° crossing.

Figure 12(b) is the compressive damage of the tunnel secondary lining under the different tunnel-fault intersection angle. It can be seen from the cloud diagram that the maximum value of the tunnel compression damage factor is basically similar at all angles of crossing. When the intersection angle between the tunnel and the fault is 90°, the maximum compression damage factor of the tunnel is distributed in the vault and the invert. With the reduction of the tunnel crossing angle, the tunnel compression damage area develops from the vault and the invert to the side walls on both sides of the tunnel and finally completely runs through. From the perspective of the distribution range of the tunnel compression damage, as the crossing angle decreases, the range of compression damage increases along the longitudinal direction of the tunnel.

Figure 13(a) shows the longitudinal distribution of OLDT along the tunnel lining under different tunnel-fault intersection angles. The abscissa in the figure represents the distance from the fault, and the positive direction of the Z-axis is positive. According to the distribution of OLDT, when the tunnel-fault intersection angle decreases, the damage area of the tunnel decreases from about 50 m at 90° crossing to about 14 m at 50° crossing, and the damage area becomes significantly smaller; the maximum value of OLDT decreases sequentially, from 0.89 reduced to 0.17 at 50° crossing. From the OLDT distribution region, except for the case of 90° and 80° crossing, the maximum damage hole segment is distributed near the fault plane. In addition to the case of 90° and 80° crossing, the OLDT value near the fault plane is larger, and the OLDT value slightly away from the fault plane is also larger. The results indicate that severe tensile damage occurs near the 90° pass and 80° pass fault plane, and severe tensile damage also occurs slightly away from the fault plane.

Figure 13(b) shows the longitudinal distribution of OLDC along the tunnel lining under different tunnel-fault intersection angles. According to the distribution of OLDT, it can be seen that under the strike-slip fault movement, the compressive damage law of each crossing angle is basically the same, and the maximum value of OLDC is concentrated near the fault plane and goes from the vicinity of the fault plane to the two sides of the tunnel; the maximum value is basically the same. From the perspective of the distribution range, when the tunnel-fault intersection angle decreases, the distribution area of OLDC increases gradually, and the damage range of OLDC increases from about 45 m at 90° to about 63 m at 50°.
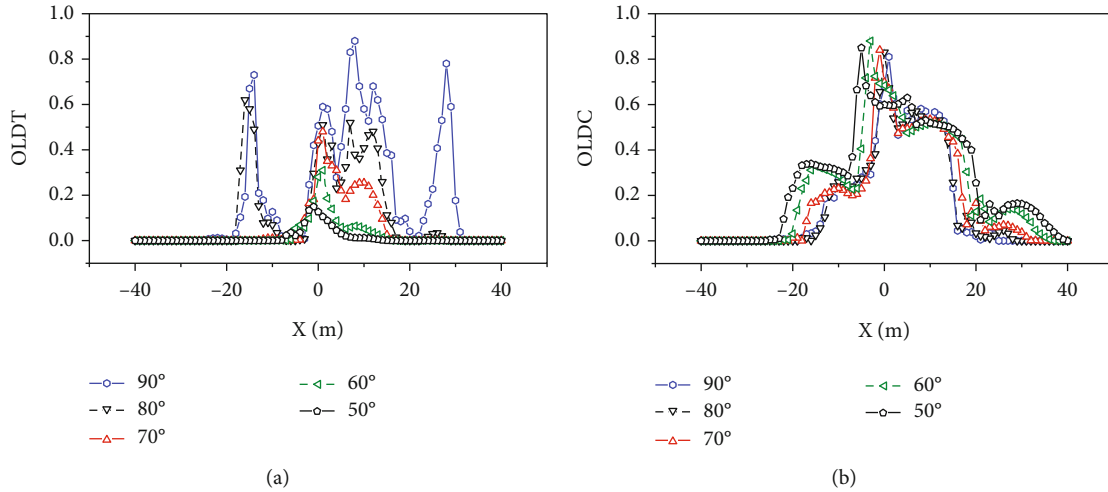
FIGURE 13: Overall lining damage under different tunnel-fault intersection angles. (a) OLDT. (b) OLTC.

6. Research Limitations and Future Work Prospects

In this paper, by establishing a three-dimensional finite element model of tunnel with strike-slip fault movement, the damage of tunnel lining under different fault plane positions, different fault displacement, and different crossing angles is discussed. Through analysis, the damage mechanism of lining under the action of active fault movement is revealed; however, the following aspects remain to be studied in this paper:

(1) In this study, the damage characteristics of the tunnel after the fault creep displacement of 30 cm were calculated through numerical simulation. Due to the limitation of the numerical model, the failure characteristics of the tunnel under the condition of several meters of fault stick-slip dislocation could not be considered

(2) This paper did not study the tectonic stress of deep buried tunnel, due to the incomplete data. Thus, the influence of tectonic stress on tunnel structure during fault dislocation remains unclear and needs to be further studied

(3) In this study, only the fault dislocation is considered, and the effect of seismic waves is not considered in the numerical model. The impact of earthquakes on the existing calculation results needs to be further studied

7. Conclusions

In the present study, a numerical model based on concrete damage plasticity model is established, and the influence of fault movements on tunnel structure is analyzed. The following conclusions can be drawn:

(1) Under the action of the maximum fault dislocation distance of 30 cm in 100 years, the fault rupture

plane may appear at anywhere in the fracture zone. When it occurs at the junction of the moving block and the fracture zone, the tensile damage, compressive damage, PQQE, and shear strain of the secondary lining show the largest values, indicating that this location is the most unfavorable fault rupture plane. In addition, the secondary lining presents serious tensile failure and shear failure under all loading conditions, and the maximum PQQE and compressive damage are concentrated in the vault and invert

(2) The axial strain of the secondary lining increases with the increase of fault displacement distance, in which the tensile strain is dominant, and the maximum tensile strain is concentrated at the fault plane and both sides of the side walls. With the decrease of the tunnel-fault intersection angle, the axial strain gradually changes from tensile strain to compressive strain, which is mainly distributed at the fault plane, and it is consistent with the direction of the tunnel-fault intersection angle

(3) The tensile and compression damage of the secondary lining increases with the increase of the fault displacement. The tensile damage of the secondary lining is mainly distributed at the fault plane and both sides of side wall of the fault plane, which develops along the tunnel circle. The compressive damage is mainly distributed at the vault and invert near the fault plane. With the decrease of the tunnel-fault intersection angle, the degree and area of tensile damage of the secondary lining are reduced, and the compressive damage area of the secondary lining develops to the side walls on both sides of the tunnel and finally completely connects

(4) The distribution length of OLDT increases from about 20 m at displacement of 5 cm to about 50 m at displacement of 30 cm, the maximum value increases from 0.18 to 0.89, the distribution length of OLDC increases from about 15 m at displacement

of 5 cm to about 45 m at displacement of 30 cm, and the maximum value increases from 0.08 to 0.81. With the decrease of the tunnel-fault intersection angle, the distribution range of OLDT decreases from about 50 m at 90° to about 14 m at 50°, the maximum value decreases from 0.89 to 0.17, and the distribution length of OLDC increases from about 45 m at 90° to about 63 m at 50°, while the maximum value is basically the same

Data Availability

The data used to support the findings of this study are available from the corresponding author upon request.

Conflicts of Interest

The authors declare that they have no conflicts of interest regarding the publication of this paper.

Acknowledgments

References

[1] Y. Wang, H. Jin, and D. T. Li, "Fault-dominated water model and multifactor method for predicting water inflow and inrush of deep long tunnel in fractured rock masses," *Chinese Journal of Rock Mechanics and Engineering*, vol. 31, no. 8, pp. 1567–1573, 2012.

[2] L. B. Chen, Q. S. Liu, and G. H. Zhang, "Prediction of inrush disaster in non-soluble rock tunnel and its engineering application," *Chinese Journal of Rock Mechanics and Engineering*, vol. 33, no. 4, pp. 786–796, 2014.

[3] Z. Y. He, J. Q. Guo, and F. Chen, "Analysis of typical disaster-causing structure and water inrush model of tunnel," *The Chinese Journal of Geological Hazard and Control*, vol. 28, no. 2, pp. 97–107, 2017.

[4] S. C. Li, Z. H. Xu, X. Huang, P. Lin, and X. C. Zhao, "Classification, geological identification, hazard mode and typical case studies of hazard-causing structures for water and mud inrush in tunnels," *Chinese Journal of Rock Mechanics and Engineering*, vol. 37, no. 5, pp. 1041–1069, 2018.

[5] B. Gao, Z. Z. Wang, S. Yuan, and Y. S. Shen, "Lessons learnt from damage of highway tunnels in Wenchuan earthquake," *Journal of Southwest Jiaotong University*, vol. 44, no. 3, pp. 336–341, 2009.

[6] X. Z. Liu and L. L. Lin, "Research on model experiment of effect of thrust fault with 75°dip angle stick-slip dislocation on highway tunnel," *Chinese Journal of Rock Mechanics and Engineering*, vol. 30, no. 12, pp. 2523–2530, 2011.

[7] X. Z. Liu, X. F. Li, Y. L. Sang, and L. L. Lin, "Experimental study on normal fault rupture propagation in loose strata and its impact on mountain tunnels," *Tunnelling and Underground Space Technology*, vol. 49, pp. 417–425, 2015.

[8] G. M. Yan, Y. S. Shen, B. Gao, Q. Zheng, and K. X. Fan, "Damage evolution of tunnel lining with steel reinforced rubber joints under normal faulting: an experimental and numerical investigation," *Tunnelling and Underground Space Technology*, vol. 97, article 103223, 2020.

[9] X. Y. Liu, C. Q. Zhang, H. B. Xiao, H. Zhou, and F. D. Chui, "Deformation and failure characteristics of a deeply buried tunnel subjected to creep slip fault movement: based on the engineering conditions of Yunnan water intake project," *Bulletin of Engineering Geology and the Environment*, vol. 81, no. 8, 2022.

[10] A. G. Chermahini and H. Tahghighi, "Numerical finite element analysis of underground tunnel crossing an active reverse fault: a case study on the Sabzkouh segmental tunnel," *Geomechanies and Geoengineering*, vol. 14, no. 3, pp. 155–166, 2019.

[11] Z. Wang, Z. L. Zhong, M. Zhao, X. L. Du, and J. Q. Huang, "Simulation of normal fault rupture and its impact on mountain tunnels," *Chinese journal of geotechnical engineering*, vol. 42, no. 10, pp. 1876–1884, 2020.

[12] S. An, L. J. Tao, J. Bian, and X. C. Han, "Damage analysis on subway tunnel structure under effect of reverse fault dislocation," *Journal Of Hunan University (Natural Science Edition)*, vol. 47, no. 7, pp. 147–156, 2020.

[13] S. An, L. J. Tao, X. C. Han, and Y. Zhang, "Application of two-level design method on subway tunnel crossing active fault: a case study on Urumqi subway tunnel intersected by reverse fault dislocation," *Bulletin of Engineering Geology and the Environment*, vol. 80, no. 5, pp. 3871–3884, 2021.

[14] X. Han and W. Li, "Numerical analysis on the structure type and mechanical response of tunnel crossing active reverse fault," *Geofluids*, vol. 2021, Article ID 5513042, 10 pages, 2021.

[15] S. Ma, Z. Liang, W. Dong, X. R. Tan, S. Li, and L. Yang, "Analysis of tunnel lining failure mechanism under the action of active fault," *Shock and Vibration*, vol. 2021, Article ID 9918021, 11 pages, 2021.

[16] GB/T 50218-2014, *GB/T 50218-2014 Standard for Engineering Classification of Rock Masses*, China Planning Press, Beijing, China, 2014.

[17] GB 50010-2010, *GB 50010-2010 Design Code for Concrete Structures*, China Architecture & Building Press, Beijing, China, 2015.

[18] Z. L. Zhong, Z. Wang, and M. Zhao, "Structural damage assessment of mountain tunnels in fault fracture zone subjected to multiple strike-slip fault movement," *Tunnelling and Underground Space Technology*, vol. 104, article 103527, 2020.

[19] C. X. Zhang, C. Yin, Y. Y. Zhang, and Z. Q. Zhang, "Analysis of damage effects of horseshoe shaped tunnel under double fault dislocation," *Railway Standard Design*, vol. 66, no. 5, pp. 106–111, 2022.

[20] H. R. Wang, Z. L. Zhong, M. Zhao, Z. Wang, X. Zhao, and D. U. Xiuli, "Model experimental study of the influence of strike-slip fault dislocation on tunnel," *Journal of Beijing University of Technology*, vol. 47, no. 7, pp. 691–701, 2021.

[21] S. An, L. J. Tao, and B. Jin, "Study on two-level design method of urban shallow subway tunnel structure crossing active fault," *Journal of Central South University (Natural Science Edition)*, vol. 51, no. 9, pp. 2558–2570, 2020.

[22] G. M. Chen, J. G. Teng, and J. F. Chen, "Finite-element modeling of intermediate crack debonding in FRP-plated RC beams," *Journal of Composites for Construction*, vol. 15, no. 3, pp. 339–353, 2011.

[23] SL 191-2008, *SL 191-2008 Design Code for Hydraulic Concrete Structures*, China Water & Power Press, Beijing, China, 2008.

[24] S. S. Shi, "Shear strength, modulus of rigidity and Young's modulus of concrete," *China Civil Engineering Journal*, vol. 32, no. 2, pp. 3–5, 1999.

[25] P. Zia, "Torsional strenth of prestressed concrete members," *ACI Journal Proceedings*, vol. 32, no. 10, pp. 1337–1359, 1961.